

Tunable enhanced spatial shifts of reflective beam on the surface of a twisted bilayer of hBN

Yu-Bo Li(李宇博), Hao-Yuan Song(宋浩元), Yu-Qi Zhang(张玉琦), Xiang-Guang Wang(王相光),Shu-Fang Fu(付淑芳), and Xuan-Zhang Wang(王选章)

Citation: Chin. Phys. B, 2022, 31 (**6**): 064207. DOI: 10.1088/1674-1056/ac3733
Journal homepage: http://cpb.iphy.ac.cn; http://iopscience.iop.org/cpb

What follows is a list of articles you may be interested in

Nonlinear optical properties in n-type quadruple δ-doped GaAs quantum wells

Humberto Noverola-Gamas, Luis Manuel Gaggero-Sager, and Outmane Oubram
Chin. Phys. B, 2022, 31 (**4**): 044203. DOI: 10.1088/1674-1056/ac248e

Improving the spectral purity of single photons by a single-interferometer-coupled microring

Yang Wang(王洋), Pingyu Zhu(朱枰谕), Shichuan Xue(薛诗川), Yingwen Liu(刘英文), Junjie Wu(吴俊杰), Xuejun Yang(杨学军), and Ping Xu(徐平)
Chin. Phys. B, 2022, 31 (**3**): 034210. DOI: 10.1088/1674-1056/ac3652

Bright 547-dimensional Hilbert-space entangled resource in 28-pair modes biphoton frequency comb from a reconfigurable silicon microring resonator

Qilin Zheng(郑骑林), Jiacheng Liu(刘嘉成), Chao Wu(吴超), Shichuan Xue(薛诗川), Pingyu Zhu(朱枰谕), Yang Wang(王洋), Xinyao Yu(于馨瑶), Miaomiao Yu(余苗苗), Mingtang Deng(邓明堂), Junjie Wu(吴俊杰), and Ping Xu(徐平)
Chin. Phys. B, 2022, 31 (**2**): 024206. DOI: 10.1088/1674-1056/ac3507

High-sensitive terahertz detection by parametric up-conversion using nanosecond pulsed laser

Yuye Wang(王与烨), Gang Nie(聂港), Changhao Hu(胡常灏), Kai Chen(陈锴), Chao Yan(闫超), Bin Wu(吴斌), Junfeng Zhu(朱军峰), Degang Xu(徐德刚), and Jianquan Yao(姚建铨)
Chin. Phys. B, 2022, 31 (**2**): 024204. DOI: 10.1088/1674-1056/ac2d20

An analytical model for cross-Kerr nonlinearity in a four-level N-type atomic system with Doppler broadening

Dinh Xuan Khoa, Nguyen Huy Bang, Nguyen Le Thuy An, Nguyen Van Phu, and Le Van Doai
Chin. Phys. B, 2022, 31 (**2**): 024201. DOI: 10.1088/1674-1056/ac2d19

Tunable enhanced spatial shifts of reflective beam on the surface of a twisted bilayer of hBN

Yu-Bo Li(李宇博), Hao-Yuan Song(宋浩元), Yu-Qi Zhang(张玉琦), Xiang-Guang Wang(王相光), Shu-Fang Fu(付淑芳)†, and Xuan-Zhang Wang(王选章)

Key Laboratory for Photonic and Electronic Bandgap Materials, Ministry of Education, and School of Physics and Electronic Engineering, Harbin Normal University, Harbin 150025, *China*

(Received 6 August 2021; revised manuscript received 18 October 2021; accepted manuscript online 6 November 2021)

We investigated Goos–Hänchen (GH) and Imbert–Fedorov (IF) shifts of a reflective beam on a twisted bilayer of hexagonal boron nitride (hBN), where a left circularly polarized beam was incident on the surface. Our results demonstrate that the twist angle between the two optical axes plays an important role in obtaining large shifts with a high reflectivity. The GH shift with $10\lambda_0$ is achieved, while the reflectivity is near 100% by tuning the twist angle. The maximum of the IF shift is found in the certain condition satisfied by the reflective coefficients, and the shift strongly depends on the twist angle between the optical axes of the two slabs. The spatial shifts obtained directly from the GH and IF shift definitions were provided, which indicate that the theoretical results from the stationary phase method are believable. These results may open up a new way for developing the nano-optical devices.

Keywords: Goos–Hänchen shift, Imbert–Fedorov shift, hBN, reststrahlen band

PACS: 42.65.–k, 81.05.Xj, 77.22.Ch **DOI:** 10.1088/1674-1056/ac3733

1. Introduction

When total internal reflection occurs, the reflection point is not the same as the incident point, which was first proven by Goos and Hänchen in 1947.[1] The displacement is in the incident plane and known as the Goos–Hänchen (GH) shift. This was explained as an experience of phase change for the reflected wave vector,[2] closely related to the interface impedance or dispersion properties. Another shift perpendicular to the incident plane is named as the Imbert–Fedorov (IF) shift,[3] which exists upon a circularly or elliptically polarized incident beam on the surface of isotropic media. The IF shift results from the interaction of the optical orbit and spin, which is one of the spin-Hall effects of light. The GH and IF shifts have been confirmed in experiments and also investigated widely in different physical systems, such as photonic crystals,[4] negative refractive media,[5] lossless dielectric slabs,[6] and others. Normally, the optical loss can be ignored for the interface between two ordinary transparent materials as well as metamaterials. In particular, the optical loss of the artificial structure obviously affects the spatial shifts, which is attributed to the optical scattering from internal defects in the material. In general, the GH shift, as well as the IF shift, is extremely weak and is not easily detected by traditional optical measurements. Therefore, a method known as the weak measurement has been established in experiments to amplify spatial shifts significantly.[8]

Many efforts have been made to enhance and tune GH and IF shifts, for instance, using various fascinating structures, i.e., left-handed metamaterials,[9] metasurfaces,[10] and anisotropic metamaterials.[11] In particular, some two-dimensional (2D) materials have been applied to investigate the spatial shifts of light, such as graphene and black phosphorus.[12,13] The chemical potential of graphene can be tuned by the gate voltage and then the adjustable and enhanced GH and IF shifts can be expected due to the coating of graphene on the surface of materials. For example, Li *et al*. experimentally measured the GH shift on the surface of a glass prism coating the graphene layer by using the beam splitter scanning method.[14] They observed a maximum difference of 31.16 μm in the GH shift between TM and TE incidences in graphene. Song *et al.* predicted large spatial shifts of the reflective beam near the critical angle and the Brewster angle on the surface of graphene/hBN metamaterial, and the reflectivity can be even more than 80%.[15] Another way to enhance the spatial shifts is to reduce the effect of optical loss. Polar crystals with lower optical loss resulting from the lattice vibration attract more attention. Most polar crystals are ionic crystals, and their reststrahlen band (RB) is different. Hexagonal boron nitride (hBN), an interesting van der Waals (vdW) crystal, is a kind of natural hyperbolic materials, which has two separate RBs. In the two RBs, the principal values of its permittivity are opposite in sign so that propagating modes are of hyperbolic dispersion. When a beam just falls in the RBs, the reflection nearly reaches the total reflection. Surface phonon polaritons (SPhPs) in ionic crystals originate from the coupling of optical phonons with electromagnetic fields. It has been proven that SPhPs in the hBN exhibit high confinement and much lower optical loss than surface plasmon polari-

†Corresponding author. E-mail: shufangfu1975@163.com

© 2022 Chinese Physical Society and IOP Publishing Ltd

tons (SPPs).[16] Thus, large spatial shifts with high reflectivity may be realized in or near the two RBs. Wang *et al.* studied the spatial shifts of the reflective beam at the critical or Brewster angle on the surface of hBN.[17] They found that the large GH shifts for s- and p-waves at the critical angle were about $-5.32\lambda_0$ and $-3.71\lambda_0$, respectively, accompanied by high reflective ratios $R_s = 0.51$ and $R_p = 0.58$. However, although the GH shift is massive at the Brewster angle, it is always accompanied by a very small reflective ratio, such as $R_p \approx 10^{-4}$. In most investigations, the optical axis (OA) is vertical or parallel to the surface, while the effect of the OA on spatial shifts has seldom been considered. In Ref. [18], a twisted structure, where the optical axes of the two hBN slabs are different in orientation, was introduced to explore the combined effects of polarization conversion and selective transmission for realizing chirality. The simulation results showed that polarization conversion in the top slab of the bilayer structure was sensitive to the tilting angle of the slab's OA. Wang *et al.* studied the influence of the orientation of OA on the GH shift of left-handed materials.[9] Wu *et al*. investigated the GH shift at the surface of the titled uniaxial crystal and noted that the permittivity expressed by the tilted angle has a remarkable effect on the shift.[19] In our recent works, the impact of the OA of hBN on the GH and IF shifts,[17] the reflection,[20] and the spin angular-momentum[21] also were further explored. Based on these discussions, it can be seen that an anisotropic dielectric permittivity can lead to complex dispersion properties because of the polarization feature of electromagnetic waves. Adjusting the spatial shifts of reflective beams by means of changing the OA orientation is promising since the change is vital to some optical devices, such as sensors and switches. In this paper, the simple bilayer structure composed of two twisted hBN slabs is considered where there is a twist angle between the two optical axes of the slabs. The twist angle effect on the two spatial shifts of the reflective beam will be investigated. Since the total reflection occurs in the RBs, we will mainly focus on the spatial shifts in these frequency bands. Then, a large spatial shift with high reflectivity may be further selected by tuning the tilted angles.

The paper is organized as follows. Section 2 shows the structure of double hBN slabs with the different OA. With the transfer method, the reflective coefficients are derived for s- and p-wave incidences, and further, the corresponding expressions of the GH and IF shifts are presented. Numerical results and discussions are in Section 3. Finally, Section 4 summarizes the entire paper.

2. Theoretical model

The structure and geometry are depicted in Fig. 1(a), where two hBN slabs with different anisotropic axes are stacked together. The optical axes of the top and bottom slabs in the x–z plane are tilted off the x-axis by angles α_1 and α_2, respectively. d_1 and d_2 represent the thicknesses of the two layers. The permittivity of hBN slabs can be expressed by

$$\overleftrightarrow{\varepsilon}_j = \begin{pmatrix} \varepsilon_{jxx} & 0 & \varepsilon_{jxz} \\ 0 & \varepsilon_{jyy} & 0 \\ \varepsilon_{jzx} & 0 & \varepsilon_{jzz} \end{pmatrix}, \tag{1}$$

where $\varepsilon_{jxx} = \varepsilon_{\parallel}\cos^2\alpha_j + \varepsilon_{\perp}\sin^2\alpha_j$, $\varepsilon_{jxz} = \varepsilon_{jzx} = (\varepsilon_{\perp} - \varepsilon_{\parallel})\cos\alpha_j \sin\alpha_j$, $\varepsilon_{jyy} = \varepsilon_{\perp}$, and $\varepsilon_{jzz} = \varepsilon_{\perp}\cos^2\alpha_j + \varepsilon_{\parallel}\sin^2\alpha_j$. Subscript $j = 1$ or 2 denotes the top or bottom slab, respectively. $\varepsilon_{\parallel}$ is the longitudinal component and $\varepsilon_{\perp}$ is the transverse component of the permittivity in the principal-axis frame. A uniform expression for $\varepsilon_{\parallel}$ or $\varepsilon_{\perp}$ is $\varepsilon_{\parallel \text{ or } \perp} = \varepsilon_{\infty}[1 + (\omega_{\text{LO}}^2 - \omega_{\text{TO}}^2)/(\omega_{\text{TO}}^2 - \omega^2 - \mathrm{i}\omega\tau_{\text{h}})]$, where $\varepsilon_{\infty} = 4.95$, $\omega_{\text{LO}} = 825$ cm^{-1} and $\omega_{\text{TO}} = 760$ cm^{-1} for the longitudinal component $\varepsilon_{\parallel}$ and $\varepsilon_{\infty} = 4.52$, $\omega_{\text{LO}} = 1610$ cm^{-1} and $\omega_{\text{TO}} = 1360$ cm^{-1} for the transverse component $\varepsilon_{\perp}$.[16] The damping coefficient is considered as $\tau_{\text{h}} = 5$ cm^{-1}. We take $f_{\text{t}} = 760$ cm^{-1} as the reference frequency for convenience. Figure 1(b) shows the real parts of $\varepsilon_{\perp}$ and $\varepsilon_{\parallel}$ as functions of frequency, and RB-I is $1.0 < \omega/f_{\text{t}} < 1.0895$ and RB-II is $1.7895 < \omega/f_{\text{t}} < 2.1184$. The hBN is the type-I hyperbolic material (HM) in RB-I, where $\varepsilon_{\perp} > 0$ and $\varepsilon_{\parallel} < 0$ and is the type-II HM in RB-II where $\varepsilon_{\perp} < 0$ and $\varepsilon_{\parallel} > 0$. The hBN exhibits elliptical or metal features in the other frequency range, where $\varepsilon_{\perp} > 0$ and $\varepsilon_{\parallel} > 0$ or $\varepsilon_{\perp} < 0$ and $\varepsilon_{\parallel} < 0$.

We consider a transverse-magnetic (TM) wave as the incident wave and the x–z plane as the incident plane since for a transverse-electric (TE) incident wave the crystal behaves like an isotropic medium due to the permittivity $\varepsilon_{\perp}$ independent of the tilted angle.[19] In addition, contrasted with the TM incidence, the GH shift produced by the TE incidence is very small. We assume the wave vector in the two slabs to be $K_j = (k_x, 0, k_{jz}^{\pm})$, and then the magnetic field in them can be expressed as

$$H_{jy} = H_{jy}^{+}\mathrm{e}^{\mathrm{i}(k_x x + k_{jz}^{+} z - \omega t)} + H_{jy}^{-}\mathrm{e}^{\mathrm{i}(k_x x + k_{jz}^{-} z - \omega t)}, \tag{2}$$

where k_{jz}^{+} and k_{jz}^{-} represent the wave vector of the up-going and down-going waves in the media. Applying $\nabla \times \boldsymbol{H} = \partial \boldsymbol{D}/\partial t$, we have

$$\begin{aligned} -\omega\varepsilon_0(\varepsilon_{jxx}E_{jx} + \varepsilon_{jxz}E_{jz}) &= (k_{jz}^{+}H_{jy}^{+} + k_{jz}^{-}H_{jy}^{-}), \\ \omega\varepsilon_0(\varepsilon_{jzx}E_{jx} + \varepsilon_{jzz}E_{jz}) &= k_x(H_{jy}^{+} + H_{jy}^{-}). \end{aligned} \tag{3}$$

From Eq. (3), we can further express the electric-field component as a function of magnetic-field component as follows:

$$E_{jx} = \frac{\varepsilon_{jzz}k_{jz}^{+} + \varepsilon_{jxz}k_x}{\omega\varepsilon_0(\varepsilon_{jxz}^2 - \varepsilon_{jzz}\varepsilon_{jxx})}H_{jy}^{+} + \frac{\varepsilon_{jzz}k_{jz}^{-} + \varepsilon_{jxz}k_x}{\omega\varepsilon_0(\varepsilon_{jxz}^2 - \varepsilon_{jzz}\varepsilon_{jxx})}H_{jy}^{-}. \tag{4}$$

From $\nabla \times \boldsymbol{E} = -\mathrm{i}\omega\mu_0\boldsymbol{H}$ and combining Eqs. (3) and (4), two solutions for k_{jz} are

$$k_{jz}^{1,2} = \left[-\varepsilon_{jxz}k_x \pm \sqrt{(\varepsilon_{jxz}^2 - \varepsilon_{jzz}\varepsilon_{jxx})(k_x^2 - k_0^2\varepsilon_{jzz})}\right]/\varepsilon_{jzz}. \tag{5}$$

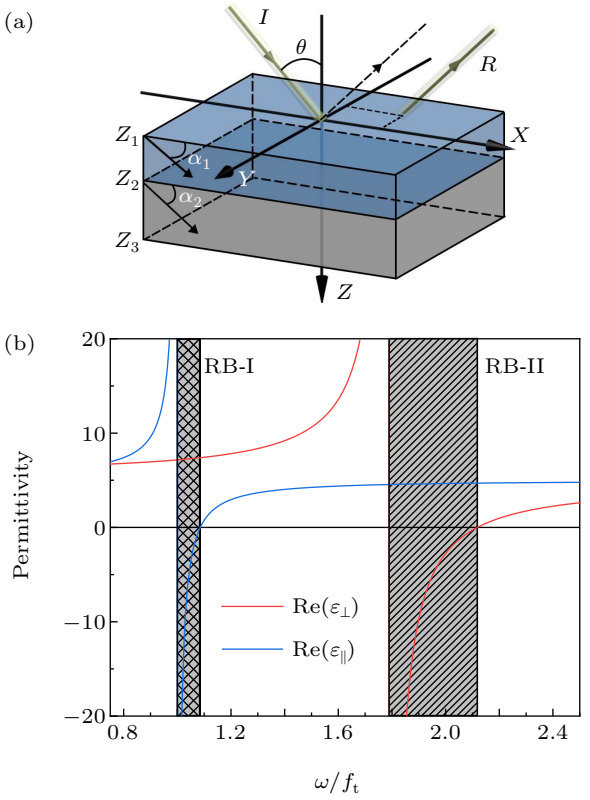


Fig. 1. (a) Schematic of twisted hBN slab structure, where the two OAs both are in the x–z plane and tilted off the x-axis by an angle α_1 for the top slab and α_2 for the bottom slab, while d_1 and d_2 represent the thicknesses of the top and bottom slabs, respectively. The incident beam with index I is at an angle θ to the z-axis. The dashed line represents the reflective beam in geometry optics, while the line with index R shows the real reflective beam. (b) The real parts of the two components of the primary permittivity as functions of the frequency. The two shadows indicate the two RBs.

The two different solutions correspond to two eigenmodes in either slab. The mode propagating from the upper surface to the bottom is defined as the down-going wave, but another propagating mode is called the up-going wave. Different from ordinary materials, the two solutions are opposite in sign to each other only when k_x is equal to zero. The properties of k_{jz} is dependent on the properties of the incident beam and material slabs. The choice of sign must guarantee the attenuation of either branch with the distance away from the crystal surface. We suppose the central incident wave with $+z$, and then we let $k_{jz}^{+} = k_{jz}^{1}$, $k_{jz}^{-} = k_{jz}^{2}$. With this hypothesis, Eq. (4) can be written as

$$E_{jx} = Z_j H_{jy}^{+} - Z_j H_{jy}^{-}, \tag{6}$$

where $Z_j = \sqrt{k_x^2 - k_0^2 \varepsilon_{jzz}}/\omega\varepsilon_0 \sqrt{\varepsilon_{jxz}^2 - \varepsilon_{jzz}\varepsilon_{jxx}}$ is called the transverse wave impedance of hBN, which has been simplified with Eq. (5). The magnetic field components outside the double-slab structure are indicated as $H_z = I e^{\mathrm{i}(k_x x + k_z z - \omega t)} + R e^{\mathrm{i}(k_x - k_z z - \omega t)}$ and $H_{\mathrm{t}z} = T e^{\mathrm{i}(k_x x + k_z z - \omega t)}$. The corresponding electric fields are summarized as $E_x = Z_0 I e^{\mathrm{i}(k_x x + k_z z - \omega t)} - Z_0 R e^{\mathrm{i}(k_x - k_z z - \omega t)}$ with $Z_0 = -\omega\mu_0 k_y/(k_x^2 + k_z^2)$ for incidence and reflection, and $E_{\mathrm{t}x} = Z_0 T e^{\mathrm{i}(k_x x + k_z z - \omega t)}$ for transmission. From the boundary conditions of the parallel components of magnetic and electric fields continuous at the surface and interface, a matrix equation governing the relation between incident and reflective or transmitted amplitudes can be derived as

$$\begin{bmatrix} I \\ R \end{bmatrix} = \Pi_0 \Pi_1 \Pi_2 \begin{bmatrix} T \\ T \end{bmatrix} = M \begin{bmatrix} T \\ T \end{bmatrix}, \tag{7}$$

where M is called the transfer matrix, including

$$\Pi_0 = \frac{1}{2Z_0} \begin{bmatrix} Z_0 + Z_1 & Z_0 - Z_1 \\ Z_0 - Z_1 & Z_0 + Z_1 \end{bmatrix}, \tag{8a}$$

$$\Pi_1 = \frac{1}{2Z_1} \begin{bmatrix} \dfrac{(Z_1 + Z_2)}{\exp(\mathrm{i}k_{1z}^{+} d_1)} & \dfrac{(Z_0 - Z_1)}{\exp(\mathrm{i}k_{1z}^{+} d_1)} \\ \dfrac{(Z_0 - Z_1)}{\exp(\mathrm{i}k_{1z}^{-} d_1)} & \dfrac{(Z_0 + Z_1)}{\exp(\mathrm{i}k_{1z}^{-} d_1)} \end{bmatrix}, \tag{8b}$$

$$\Pi_2 = \frac{1}{2Z_1} \begin{bmatrix} \dfrac{(Z_2 + Z_3)}{\exp(\mathrm{i}k_{2z}^{+} d_2)} & 0 \\ 0 & \dfrac{(Z_2 + Z_3)}{\exp(\mathrm{i}k_{2z}^{-} d_2)} \end{bmatrix}. \tag{8c}$$

Now we consider the effect of the imaginary part of $k_{jz}^{1,2}$ in the transfer matrix. We take $\alpha_1 = \alpha_2 = 0^\circ$ as an example and plot the imaginary part of $k_{jz}^{1,2}$ versus the frequency, as shown in Fig. 2. Two clear jumping points are found at $\omega/f_{\mathrm{t}} = 1.8$ and 2.1, which are just at the boundary of RB-II. From the inset, the first jumping point at the left boundary is that the imaginary part of k_{jz}^{1} changes from a positive value to a negative one, and meanwhile the imaginary part of k_{jz}^{2} becomes positive. Another jumping happens at the right boundary and the situation is exactly opposite to the first jumping. Thus, in RB-II, k_{jz}^{1} becomes negative and k_{jz}^{2} is positive, which is not consistent with the above assumption. Therefore, we have to modify the transfer matrix M using $k_{jz}^{+} = k_{jz}^{2}$, $k_{jz}^{-} = k_{jz}^{1}$ in Eq. (7) to keep the attenuation along propagation directions.

The reflective coefficient r_{p} is obtained from the transfer matrix M as follows:

$$r_{\mathrm{p}} = \frac{M(2,1) + M(2,2)}{M(1,1) + M(1,2)} \tag{9}$$

for the TM component in the reflective wave, and another reflectivity coefficient can be written as

$$r_{\mathrm{s}} = \frac{r_1 + r_2 \exp(2\mathrm{i}k_{oz} d)}{1 + r_1 r_2 \exp(2\mathrm{i}k_{oz} d)} \tag{10}$$

for the TE component of the reflective wave, where $r_1 = (k_z - k_{oz})/(k_z + k_{oz})$ and $r_2 = (k_{oz} - k_z)/(k_z + k_{oz})$ represent the reflection coefficients at the upper surface and interface between the two slabs, respectively. Also, the wave vector along the z-axis $k_{oz} = \sqrt{\mu_0 \omega^2 \varepsilon_\perp - k_x^2}$ in the two slabs. Comparing Eqs. (9) and (10), it can be seen that r_{p} is related not only to $\varepsilon_\parallel$ and $\varepsilon_\perp$ but also to the titled angles α_1 and α_2, but r_{s} only depends on $\varepsilon_\perp$. Therefore, in the following discussions,

we will only focus on the GH shift for the p-wave reflective coefficient. According to Eq. (9), the GH shift is[22,23]

$$\Delta x_{\mathrm{p}} = -\frac{\lambda_0}{2\pi\cos\theta}\frac{\partial\varphi_{\mathrm{p}}}{\partial\theta}, \tag{11}$$

by means of the stationary phase method, where λ_0 is the vacuum wavelength. Obviously, the GH shift can reach its peak when the phase difference φ_{p} experiences a sharp variation with the incident angle. Therefore, the massive GH shift can be observed near the Brewster angle or the critical angle.

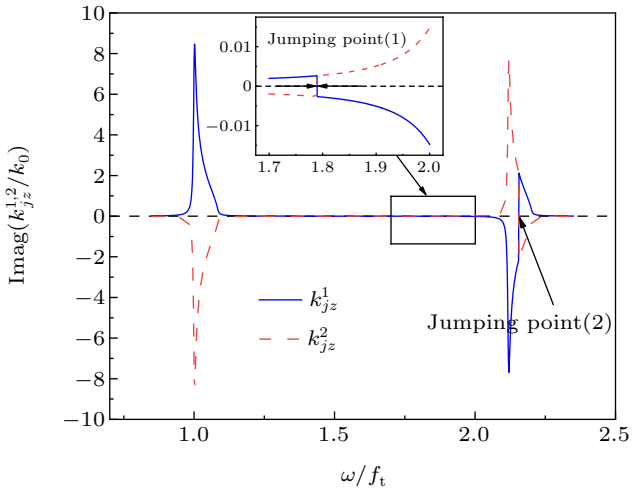


Fig. 2. Imaginary part of $k^{1,2}_{jz}$ $(j=1,2)$ of the mode wave versus frequency at $\alpha_1=\alpha_2=0°$. The inset shows the first jumping point at $\omega/f_{\mathrm{t}}=1.8$, where the imaginary part of k^1_{jz} becomes negative and k^2_{jz} becomes positive. The second jumping point happens at $\omega/f_{\mathrm{t}}=2.1$, where the signs of k^1_{jz} and k^2_{jz} are swapped.

Contrary to the longitudinal GH shift, the IF shift is a transverse shift perpendicular to the incident plane. We assume that the incident beam is left circularly polarized (LCP) and define the electric field of the central ray in this beam as $E_{\mathrm{i}}=E^{\mathrm{p}}_{\mathrm{i}}-\mathrm{i}E^{\mathrm{s}}_{\mathrm{i}}$. The reflective beam also is a paraxial beam and its IF shift is independent of the profile of the beam if the beam waist is large enough. The IF shift of the reflective beam can be written as[24]

$$\Delta y_{\mathrm{LCP}} = -\frac{\lambda_0\cot\theta}{2\pi}\left[1+2\cos(\varphi_{\mathrm{s}}-\varphi_{\mathrm{p}})\frac{|r_{\mathrm{p}}||r_{\mathrm{s}}|}{|r_{\mathrm{p}}|^2+|r_{\mathrm{s}}|^2}\right], \tag{12}$$

where $\varphi_{\mathrm{p}}-\varphi_{\mathrm{s}}$ is the phase difference between the reflective coefficients r_{p} and r_{s}. Moreover, it is seen from Eq. (12) that the maximum of the IF shift $\Delta y_{\max}=-\lambda_0\cot\theta/\pi$ in the condition of $|r_{\mathrm{p}}|=|r_{\mathrm{s}}|$ and $\varphi_{\mathrm{p}}-\varphi_{\mathrm{s}}=2n\pi$ (n is an integer). In a recent work, the peak values in graphene/hBN metamaterials were obtained through tuning the chemical potential of graphene and the incident angle.[15] After checking the expressions of the reflective coefficients [see Eqs. (9) and (10)], we found that the condition in the twisted structure mainly depends on the choice of the titled angles of the OAs when the incident angle is fixed.

3. Results and discussion

3.1. GH shift of the reflective beam

We take the thicknesses of the top and bottom slabs as 1.5 μm and 2.5 μm, respectively. Unlike the hyperbolic metamaterials, hBN is a nature hyperbolic material, so the spatial shifts can be further enhanced only by promoting the quality of the hBN crystal. We will investigate the large GH shift accompanied with the high reflectivity in the RBs. The incident angle is fixed at $\theta=85°$ in subsequent discussions since the large GH shift may be achieved at large incident angles, as indicated by Eq. (11). The effect of the OA orientations on the GH shift in the RBs also will be discussed, where the titled angle of the top OA is taken as $\alpha_1=0°$, 30°, and 90°, respectively. For $\alpha_1=0°$, the GH shift distribution as a function of frequency and tilted angle α_2 in RB-I is presented in Fig. 3(a). It can be found that the positive maximum is about $38\lambda_0$, localized at the left boundary of RB-I and in the range of $\alpha_2>30°$, while the negative maximum is about $-5\lambda_0$, appearing at the right boundary and the range of $\alpha_2>80°$. Two obvious intersecting strips with relatively high GH shift values are observed. Contrasting with the reflectivity shown in Fig. 3(b), unfortunately in these regions the reflectivity becomes very small. Near the maximum GH shift value, an impressive GH shift with about 30% reflectivity can be acquired, which is not bounded by the tilted angle α_2. The GH shift reduces evidently as the frequency is increased, but reflectivity is enhanced, by more than 70% in some regions. For example, $R\approx75\%$ and $\Delta x\approx15\lambda_0$ for $\omega/f_{\mathrm{t}}=1.02$ and $\alpha_2=20°$. Thus, the purpose to directly heighten the reflective ratio by means of slightly sacrificing the shift value can be realized. For $\alpha_1=30°$, the vertical strip with a larger GH shift moves to the middle of the frequency window, as shown in Fig. 3(c). Moreover, the GH shift is enhanced significantly. Contrasted with Fig. 3(d), the GH shift in the frequency range of $\omega/f_{\mathrm{t}}>1.02$ should be paid more attention since the reflectivity is more than 60% except for the strip zone. Of course, the negative GH shift is expected in the region of $\omega/f_{\mathrm{t}}<1.01$ and $\alpha_2>30°$. For $\alpha_1=90°$, the maximum of the GH shift quickly drops to about $19\lambda_0$, lower than the other two cases, as shown in Fig. 3(e). However, it is interesting that the reflectivity shown in Fig. 3(f) is evaluated to be more than 30% in the whole region. In this case, we can arbitrarily choose the GH shift value according to the requirement without the consideration of reflectivity.

Now we focus on the GH shift and reflectivity in RB-II, as presented in Fig. 4. The large GH shift near the strip attracts our attention due to nearly 100% reflectivity in a certain region at $\alpha_1=0°$. For example, $\Delta x\approx10\lambda_0$ with $R\approx0.96$ for $\omega/f_{\mathrm{t}}=1.8$ and $\alpha_2=85°$. The situation of $\alpha_1=30°$ is a little complicated due to the intersection of two strips. Although a massive GH shift over 100 times the vacuum wavelength is ob-

served at a narrow frequency band, the corresponding reflectivity is very low, almost close to zero. In the other region, to obtain the large GH shift with high reflectivity is also difficult. An interesting phenomenon should be noted when $\alpha_2 = 90°$. Comparing Figs. 4(e) and 4(f), a GH shift accompanied with high reflectivity is obtained in a wide frequency range. For instance, the GH shift about $20\lambda_0$ with 70% reflectivity is easily achieved.

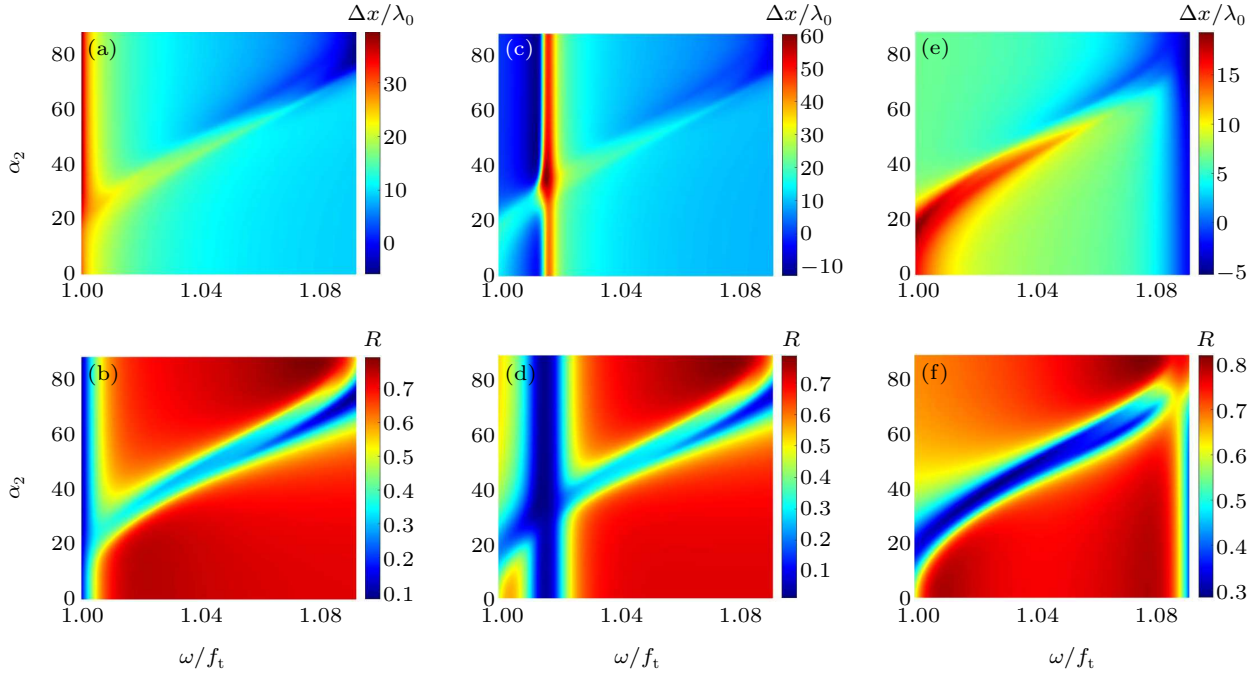


Fig. 3. GH shift and reflectivity versus frequency and bottom titled angle α_2 in RB-I: (a) and (b) for $\alpha_1 = 0°$, (c) and (d) for 30° and (e) and (f) for 90°.

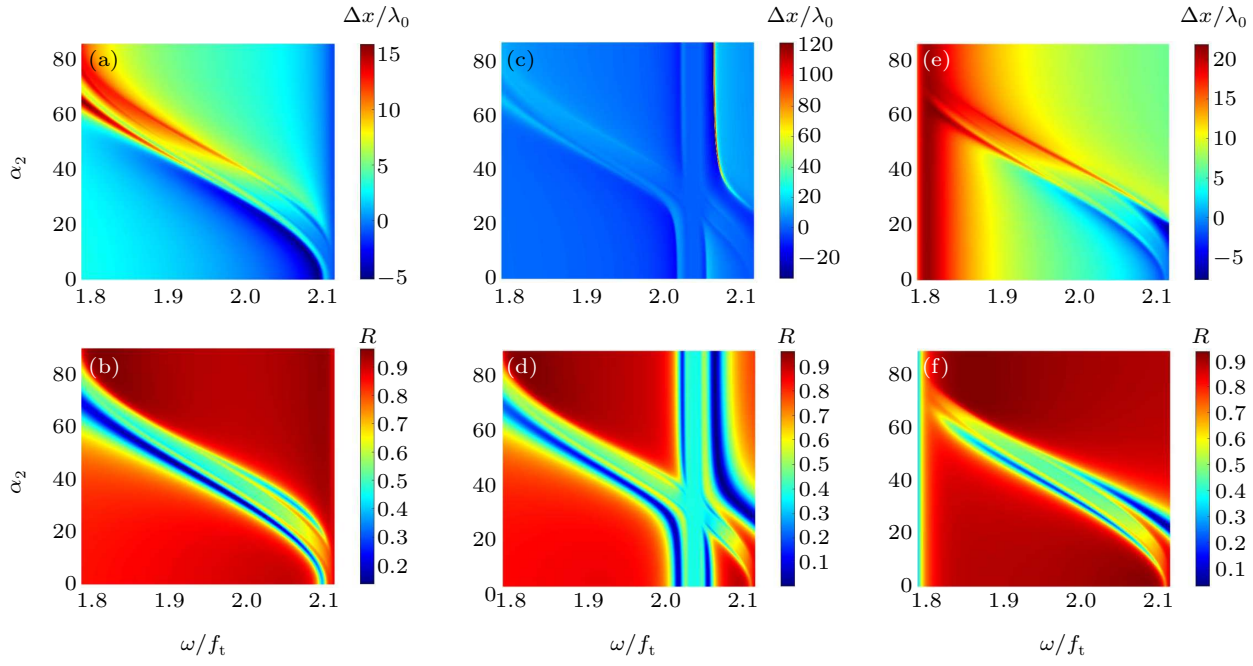


Fig. 4. GH shift and reflectivity versus frequency and bottom titled angle α_2 in RB-II: (a) and (b) for $\alpha_1 = 0°$, (c) and (d) for 30° and (e) and (f) for 90°.

In order to further indicate the effect of α_1 and α_2 on the GH shift, the GH shift and reflectivity spectra at $\omega/f_t = 1.05$, 1.08 in RB-I are depicted in Fig. 5. An obvious intersection of the two strips is discovered and divides the frequency window into four parts. Among them, the region of $\alpha_1 < 52°$ and $\alpha_2 < 52°$ attracts attention, where the GH shift is about $10\lambda_0$ and the reflectivity is over 50%. It is worth noting that this region is expanded as the frequency increases to $\omega/f_t = 1.08$, as shown in Figs. 5(c) and 5(d). Figures 3–5 show two distinct intersecting strips in which the GH shift is large but the reflec-

tivity is very small. Based on the discussion for the derivation of the phase difference with the incident angle in Eq. (11), the incident angles related to these regions should be near Brewster angles, where the reflectivity is almost zero. If we further examine the wave vector of either hBN slab (see Eq. (5)), it can be found that the two absorption strips in the reflective spectra will be mainly determined by the twist angle of the OA orientation of the two slabs.

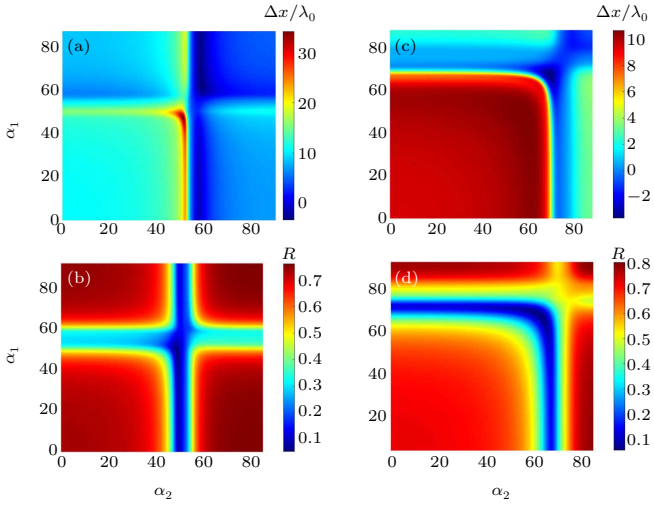


Fig. 5. GH shift and reflectivity versus titled angles α_1 and α_2: (a) and (b) at $\omega/f_t = 1.05$, and (c) and (d) at $\omega/f_t = 1.08$.

3.2. IF shift of the reflective beam

In this part, the distribution of the IF shift versus the titled angles and the frequency is indicated in Fig. 6. The incident angle is fixed at $\theta = 10^\circ$ in the following numerical calculation. Due to Eq. (12), the maximum of the IF shift, $\Delta y_{\max} = -\lambda_0 \cot\theta/\pi$, is about $-1.8\lambda_0$ in the conditions mentioned above. Firstly, we consider the changes of the IF shift versus α_2 when $\alpha_1 = 0^\circ$, 60°, and 90°, as shown in Figs. 6(a)–6(c). For $\alpha_1 = 0^\circ$, the maximum of the IF shift is found in RB-II and the region with the maximum gradually shrinks and moves to the lower frequency region with an increase of α_1. When $\alpha_1 = 60^\circ$, the relatively larger values appear not only in RB-II but also in RB-I. However, the frequency bands with large IF shifts are very narrow. We further twist the upper hBN plate to 90°. It is found that the maximum of the IF shift in RB-II completely transfers into RB-I, and is slightly smaller than the other two cases. This implies that the conditions obtaining the maximum cannot be matched in RB-I. Secondly, the titled angle of the bottom hBN is fixed at $\alpha_2 = 0^\circ$, 30°, and 90°, as shown in Figs. 6(d)–6(f). Unlike the first case, the region with the large IF shift is found in RB-I and gradually moves to RB-II. As shown in Fig. 6(e), the IF shift in RB-I is smaller than that in RB-II. As α_2 is increased to 90°, the blue region with the maximum of IF shift moves into RB-II entirely. Comparing the two cases, it can be easier to get the maximum of the IF shift at the second case. When carefully checking the changes of the IF shift with α_1 and α_2, we find that the twist angle of the OA orientation between the two hBN slabs plays an important role.

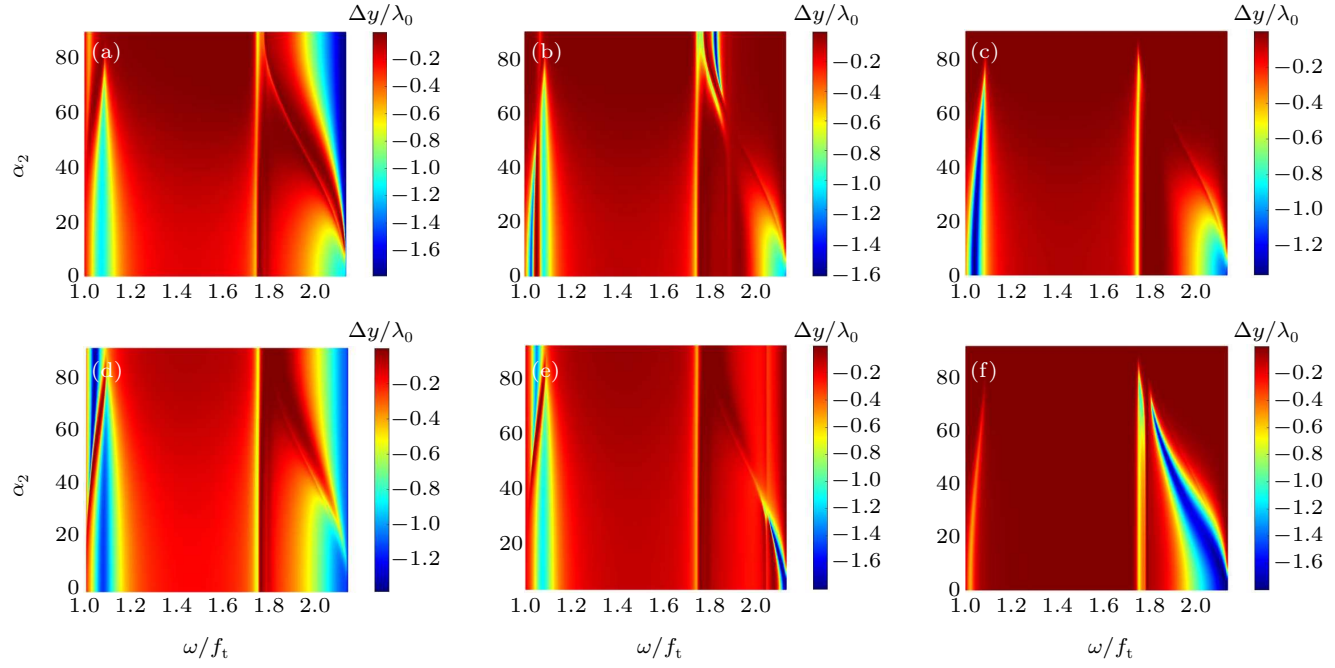


Fig. 6. IF shift in RBs versus frequency and tilted angles: (a)–(c) show IF shift at $\alpha_1 = 0^\circ$, 60°, 90°; (d)–(e) show IF shift at $\alpha_2 = 0^\circ$, 30°, 90°.

In the following, we further investigate the effect of the twist angle on the conditions for obtaining the largest IF shift, as shown in Fig. 7. The maximum of IF shift is found in RB-II. The phase or reflectivity difference for p- and s-waves met with the conditions $\varphi_p - \varphi_s = 0$ and $|r_p| = |r_s|$ at some special titled angles, which are exhibited by the perpendic-

ular dot lines. It is noted that the maximum of the IF shift can be obtained at the expected frequency by tuning the tilted angles of the two slabs properly. For example, the maximum of the IF shift can be obtained at $\alpha_1 = 3°$ and $\alpha_2 = 50°$ for $\omega/f_t = 2.127$, and also at $\alpha_1 = 10°$ and $\alpha_2 = 40°$ for $\omega/f_t = 2.144$.

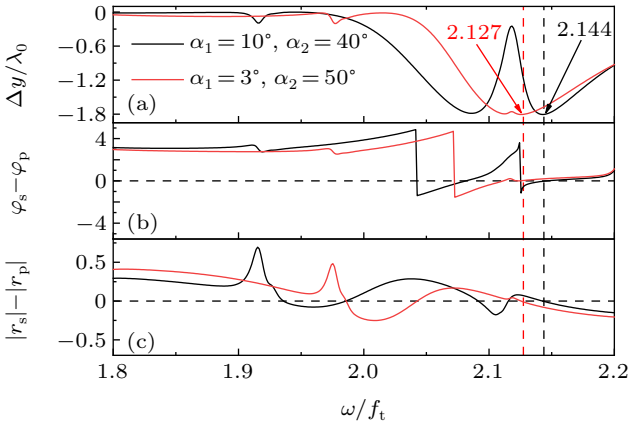


Fig. 7. (a) IF shift, the difference of (b) phase or (c) reflectivity between p- and s-waves versus frequency under the condition of $\alpha_1 = 3°$ and $\alpha_2 = 50°$ or $\alpha_1 = 10°$ and $\alpha_2 = 40°$.

3.3. Beam simulations for GH and IF shifts of reflected Gaussian beam

From the above analysis and considering a paraxial incident beam, an assumption is necessary, which is that the phase of the reflectivity coefficient is a linear function of the in-plane wave vector in the cross section of the incident beam. In reality, the incident Gaussian beam should be with a finite waist. Therefore, a comparison is made between the results using the beam simulation and the ones obtained with the stationary phase method. The Gaussian incident beam with the waist width W_0 and TM-polarization considered here is expressed by

$$E_i = W_0 \exp(-W_0^2 \boldsymbol{k}_\perp^2/4)/\sqrt{2\pi}, \tag{13}$$

where $\boldsymbol{k}_\perp$ represents the difference between any wave vector and the central wave vector in the incident beam. The field profile of the reflected beam can be presented as follows:

$$E_r = \frac{1}{2\pi}\int_{-\infty}^{+\infty} R(\boldsymbol{k}_\perp)\bar{E}_i(\boldsymbol{k}_\perp)e^{i\boldsymbol{k}_\perp \cdot r}\mathrm{d}\boldsymbol{k}_\perp. \tag{14}$$

Thus, the GH and IF shifts can be described by[15,25]

$$\Delta x = \frac{\int_{-\infty}^{+\infty} E_r^* \frac{i\partial}{\partial k_t} E_r \mathrm{d}\boldsymbol{k}_\perp}{\int_{-\infty}^{+\infty} E_r^* E_r \mathrm{d}\boldsymbol{k}_\perp}, \quad \Delta y = \frac{\int_{-\infty}^{+\infty} E_r^* \frac{i\partial}{\partial k_p} E_r \mathrm{d}\boldsymbol{k}_\perp}{\int_{-\infty}^{+\infty} E_r^* E_r \mathrm{d}\boldsymbol{k}_\perp}. \tag{15}$$

Here, k_t and k_p specify the in-plane and out-of-plane deflection of non-central wave and E_r represents the electric field of the reflected beam.

Figure 8(a) represents the GH shift versus the titled angle α_1 for the different α_2 in RB-I at $\omega/f_t \approx 1.05$ and $\theta = 85°$. The maximal values are about $\Delta x \approx 32\lambda_0$ at $\alpha_1 = 50.27°$ and $\alpha_2 = 50°$ and $\Delta x \approx 18\lambda_0$ at $\alpha_1 = 51.89°$ and $\alpha_2 = 90°$, respectively. Figure 8(b) simulates the GH shift versus the waist of the incident beam at the conditions for obtaining the maximal shift values shown in Fig. 8(a). It is evident that the GH shift will be steady after the waist width relative to the vacuum wavelength is larger than a certain value, which just coincides with the results in Fig. 8(a) from the stationary phase method. In Fig. 9(a), the IF shift as a function of α_1 is presented at $\omega/f_t = 2.08$, $\alpha_2 = 40°$ and $\theta = 10°$. Two points, $\alpha_1 = 12.79°$ and 18.96°, are chosen in Fig. 9(a), and the curves of IF shift versus the waist at the two points are depicted in Fig. 9(b). Compared with Fig. 9(a), the IF shift obtaining from the two ways also agrees well if the beam waist is large enough.

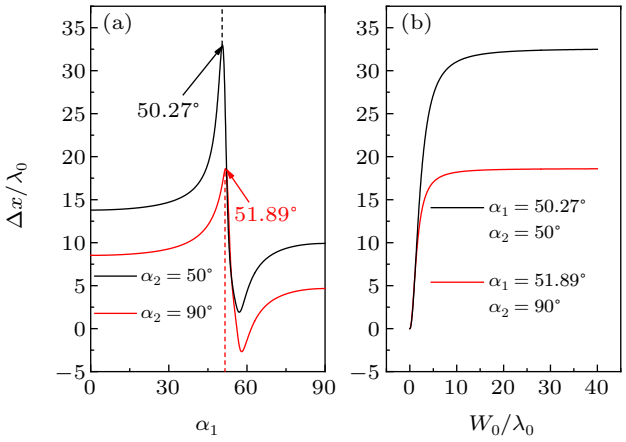


Fig. 8. Comparison of the GH shift between the stationary phase method and the beam simulation at $\omega/f_t = 1.05$ and $\theta = 85°$. GH shift versus (a) α_1 at $\alpha_2 = 50°$ and 90° and (b) W_0/λ_0 at $\alpha_1 = 50.27°$ and $\alpha_2 = 50°$ for the black curve and $\alpha_1 = 51.89°$ and $\alpha_2 = 90°$ for the red curve.

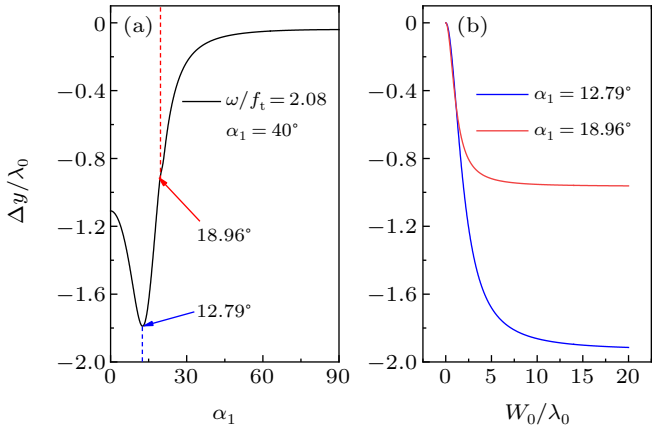


Fig. 9. Comparison of IF shift between the stationary phase method and the beam simulation at $\omega/f_t = 2.08$, $\alpha_2 = 40°$ and $\theta = 10°$. (a) IF shift versus α_1. (b) IF shift versus W_0/λ_0 at $\alpha_1 = 12.79°$ and 18.96°.

4. Conclusion

We took advantage of a planar bilayer structure composed of two twisted hBN slabs to realize the large spatial shifts with high reflectivity. The GH and IF shifts of the reflective beam on the surface were numerically calculated as functions of the OA orientations in the two hBN slabs. Interesting phenomena

are that the GH shift can reach about $10\lambda_0$ with near 100% reflectivity in some cases, and the maximum of the IF shift appears alternately in the two RBs by tuning the titled angles of the OAs. The conditions obtaining the maximum of IF shift, $\varphi_s = \varphi_p$ and $|r_s| = |r_p|$, were discussed and it is found that they strongly depend on the twist angle between the optical axes of the two slabs. Finally, the results from the beam simulation are provided to make a contrast with the ones from the stationary phase method. This is acceptable when the beam waist is large enough, compared with the wavelength. The twisted structure built with the nature hBN is simple, however, the directly measured spatial shifts are impressive. The results of this work may be beneficial to the design of nano-optical devices and applications in infrared regions.

Acknowledgments

Project supported by the Natural Science Foundation of Heilongjiang Province, China (Grant No. LH2020A014), Harbin Normal University Fund (Grant No. HSDSSCX2021-27), and Education Commission of Heilongjiang Province, China (Grant No. 2020-KYYWF352).

References

[1] Goos F and Hänchen H 1947 *Ann. Phys.* **436** 333
[2] Goos F and Hänchen H 1949 *Ann. Phys.* **5** 251
[3] Fedorov F I 1955 *Dokl. Akad. Nauk SSSR* **105** 465
[4] Wang L G and Zhu S Y 2010 *Appl. Phys. B* **98** 459
[5] Chen L, Cao Z Q, Zhang D W, Zhu Y M and Zhuang S L 2009 *Proceedings of SPIE-The International Society for Optical Engineering* **7279** 15
[6] Piper J R and Fan S H 2014 *ACS Photon.* **1** 347
[7] Abergel D S L, Apalkov V, Berashevich J, Zieg L K and Chakraborty T 2010 *Adv. Phys.* **59** 261
[8] Hosten O and Kwiat P 2008 *Science* **319** 787
[9] Wang, Li G and Zhu S Y 2005 *J. Appl. Phys.* **98** 043552
[10] Ziauddin, Chuang Y L, Sajid Q and Lee R K 2016 *Sci. Rep.* **6** 26504
[11] Huang Y Y, Zhao B and Gao L 2012 *J. Opt. Soc. Am. A* **29** 1436
[12] Madani A and Entezar S R 2015 *Superlattices and Microstructures* **86** 105
[13] Low T, Rodin A, Carvalho A, Jiang Y, Wang H, Xia F and Neto A C 2014 *Phys. Rev. B* **90** 075434
[14] Li X, Wang P, Xing F, Chen X D, Liu Z B, Tian J G 2014 *Opt. Lett.* **39** 5574
[15] Song H Y, Fu S F, Zhang Q, Zhou S and Wang X Z 2021 *Opt. Express* **29** 19068
[16] Fu S F, Zhou S, Zhang Q and Zhang W X 2020 *Opt. Laser Technol.* **125** 106012
[17] Wang X G, Zhang Y Q, Zhou S, Fu S F and Wang X Z 2020 *Opt. Express* **28** 25048
[18] Wu X H, Fu C J and Zhang Z M 2019 *Opt. Commun.* **452** 124
[19] Wu X H 2018 *Opt. Commun.* **416** 181
[20] Zhou S, Abdullah K, Fu S F and Wang X Z 2019 *Opt. Express* **27** 15222
[21] Zhang Y Q, Wang X G, Zhang D Z, Fu S F, Zhou S and Wang X Z 2020 *Opt. Express* **28** 19205
[22] Wang L G, Chen H and Zhu S Y 2005 *Opt. Lett.* **30** 2936
[23] Kong Q, Shi H, Shi J and Chen X 2019 *Opt. Express* **27** 11902
[24] Xu C R, Xu J P, Song G, Zhu C J, Yang Y P and Agarwal G 2016 *Opt. Express* **24** 21767
[25] Bliokh K Y and Aiello A 2013 *J. Opt.* **15** 014001